Physical Observation of a Robust Acoustic Pumping in Waveguides with Dynamic Boundary

Xianchen Xu, ^{1,*} Qian Wu, ^{1,*} Hui Chen, ^{1,*} Hussein Nassar, ¹ Yangyang Chen, ¹

Andrew Norris, ² Michael R. Haberman, ³ and Guoliang Huang, ^{1,†}

¹Department of Mechanical and Aerospace Engineering, University of Missouri, Columbia, Missouri 65211, USA, ²Mechanical and Aerospace Engineering, Rutgers University, Piscataway, New Jersey 08854-8058, USA, ³Walker Department of Mechanical Engineering and Applied Research Laboratories, The University of Texas at Austin, Austin, Texas 78712, USA

(Received 29 June 2020; accepted 11 November 2020; published 15 December 2020)

Research on breaking time-reversal symmetry to realize one-way wave propagation is a growing area in photonic and phononic crystals and metamaterials. In this Letter, we present physical realization of an acoustic waveguide with spatiotemporally modulated boundary conditions to realize nonreciprocal transport and acoustic topological pumping. The modulated waveguide inspired by a water wheel consists of a helical tube rotating around a slotted tube at a controllable speed. The rotation of the helical tube creates moving boundary conditions for the exposed waveguide sections at a constant speed. We experimentally demonstrate acoustic nonreciprocity and topologically robust bulk-edge correspondences for this system, which is in good agreement with analytical and numerical predictions. The nonreciprocal waveguide is a one-dimensional analog to the two-dimensional quantum Hall effect for acoustic circulators and is characterized by a robust integer-valued Chern number. These findings provide insight into practical implications of topological modes in acoustics and the implementation of higher-dimensional topological acoustics where time serves as a synthetic dimension.

DOI: 10.1103/PhysRevLett.125.253901

The law of reciprocity is a fundamental principle and design constraint of waves and vibrations control in linear, time-invariant systems that require energy transport between two points in space to be symmetric. Thus, reciprocity can be a hindrance in systems where asymmetric wave motion is sought. For example, one-way acoustic devices, such as three-port circulators [1] and one-way diodes [2], cannot exist with unbroken reciprocity [3–8]. Creating nonreciprocal materials and devices has therefore attracted tremendous attention for enabling unidirectional energy transport [9–17], topological insulators [18,19], and edge modes [20,21]. Many strategies, including strongly nonlinear networks [22–26], gyroscopic media [27,28], circulating fluids [29,30], and spatiotemporally modulated materials [31–39], have been proposed. Among them, spatiotemporal modulation by introducing a temporal topological pumping has been widely investigated in active elastodynamic systems. However, the physical realization of the temporal pumping generally requires sophisticated external fields or smart materials applied in the system. For example, nonreciprocity induced by electromechanical pumping was recently experimentally demonstrated by introducing a periodic array of electromagnets on a beam to control positive and negative propagating mechanical waves [31]. A similar approach was adopted experimentally by proposing a magnetomechanical topological insulator to demonstrate the temporal pumping that produces robust mechanical energy transport [38]. Surprisingly, compared with their mechanical counterparts, there are few works on physical evidence of spatiotemporal pumping in acoustics, not to mention the nonreciprocal and topological transport of acoustic waves.

In this Letter, we propose a 1D dynamic waveguide that displays nonreciprocal wave phenomena without imposing external fields to modulate the acoustic properties in space and time. Rather, we employ a novel paradigm whereby the bulk properties are left intact, while the boundary conditions are, through purely mechanical means, modulated in space and time. This is achieved by mounting a helical tube on a slotted acoustic waveguide and then rotating the helix with a motor, as shown in Fig. 1(a). This configuration is shown to be capable of pumping acoustic energy unidirectionally in a manner reminiscent of a water wheel. The system results in an acoustic waveguide with exposed holes (shunts) that are effectively translated at a constant speed along the axis of the waveguide when the helical tube is rotated by the motor. It is worth noting that, while the properties of the tube are time independent, the boundary conditions and therefore the impedance of the waveguide is indeed time dependent, leading to the "dynamic" waveguide [31]. This strategy differs from the acoustic pumping where wavelike modulations of constitutive parameters are utilized to study parametric amplification in the unstable regime [40]. As a result, the modulated acoustic waveguide

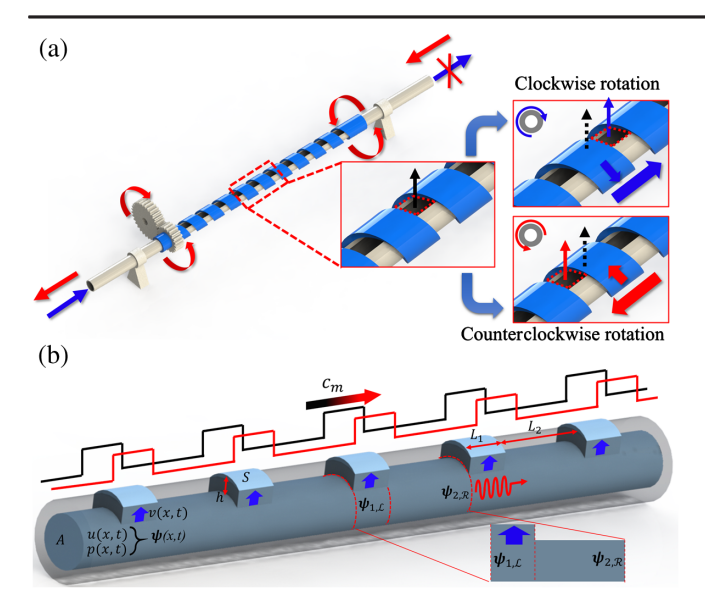


FIG. 1. (a) Schematic illustration of the modulated acoustic waveguide. A fixed, slotted tube (gray) with a long straight opening is inserted into a helical tube (blue), forming an array of parallelogram openings in the acoustic waveguide. The helical tube is driven mechanically by a motor system. Clockwise and counterclockwise rotations realize forward and backward spatiotemporal modulation, respectively, as the exposed sections translate, indicated by the insets. (b) Schematic of the equivalent spatiotemporally modulated medium. The gray and light blue regions represent the rigid material and air, respectively. The moving exposed sections enable the spatiotemporal modulation of waveguide boundary conditions. p(x,t) and u(x,t) represent the longitudinal pressure and velocity fields in the tube, " \mathcal{R} " and " \mathcal{L} " denote the right and left interfaces of the unit cell, respectively.

supports nonreciprocal acoustic energy transport and acoustic topological pumping. We experimentally demonstrate the nonreciprocal acoustic wave propagation when the modulation speed is small compared to the sound speed in the waveguide and that the frequency range of nonreciprocity can be tuned by changing the angular velocity of the helix. We further experimentally illustrate the acoustic topological bulk-edge correspondence under different boundary conditions. The experimental results are in good agreement with analytical predictions and numerical simulations.

Theoretical predictions of wave behavior in the proposed system are conducted by modeling the acoustic tube with moving, exposed sections (ESs) as a two-phase medium with translating phases, as shown in Fig. 1(b). Rotation of the helical tube results in a linear speed c_m of the ESs relative to the acoustic waveguide reference frame. The boundary condition of the acoustic waveguide is hence time dependent with a nonzero modulation speed $c_m = \omega_m/k_m$. In this scenario, the air column moves in and out through the ESs at a modulated vertical velocity $v(x,t) = V\{1 + \exp[-\mu\cos(\omega_m t - k_m x) - \mu\cos(\pi y)]\}^{-1}$,

driven by the pressure p(x,t) in the ESs according to Newton's law $p(x,t)S = M\partial_t v(x,t)$ [41]. Here $\mu = 5$ is chosen, which does not necessarily influence the numerical results but optimizes the numerical convergence (Supplemental Material [42], Sec. A). The ES acts as a sink that modifies the equations of motion in the ES,

$$-\left(\frac{1}{B}\right)\partial_t p(x,t) = \partial_x u(x,t) + \left(\frac{\sigma_1}{A}\right)v(x,t), \quad (1)$$

$$-\partial_x p(x,t) = \rho \partial_t u(x,t), \tag{2}$$

where A denotes the tube cross-sectional area, B and ρ are the bulk modulus and density of air, respectively, $\sigma_1 = NS$ with $N = (L_1 + L_2)^{-1}$, and $M = \rho Sh$. While for the nonexposed section, the general equations of motion read

$$-\left(\frac{1}{B}\right)\partial_t p(x,t) = \partial_x u(x,t),\tag{3}$$

$$-\partial_x p(x,t) = \rho \partial_t u(x,t). \tag{4}$$

We utilize the transfer matrix method to visit the acoustic nonreciprocal regime for various modulation speeds c_m (see Supplemental Material [42], Sec. A for derivation details). The effect of slow modulations (the modulation frequency is smaller than the bandwidth) is to shear the dispersion curves and create a couple of directional band gaps. The emergence of the direction gaps is the direct observation of the band-tilting-induced nonreciprocity.

Progressive modulation in various modulation frequency regions creates a bias in space and time, which enables nonreciprocal wave propagation as a function of modulation frequency and depth. For a small modulation speed, the phase shift induced by adiabatic pumping over a short time period is insufficient to trigger any intermodal transitions and the band structure gets sheared and tilted to create a directional band gap [8,43]. For a smallamplitude and moderate modulation speed, Bragg scattering due to time-dependent interface causes the frequency shift for scattered waves, which is related to Doppler shifting [45]. Figure 2(a) illustrates the theoretical dispersion relations of the modulated waveguide with a small modulation speed $c_m = 0.029c_0$, where the modulation frequency ($\omega_m = 20 \text{ rad/s}$) is much smaller than the width of the first band gap ($\delta\omega = 160 \text{ rad/s}$). In this example, the geometric parameters are $L_1 = 0.01$ m, $L_2 = 0.03 \text{ m}, \quad S = L_1^2 = 1 \times 10^{-4} \text{ m}^2, \quad \sigma_1 = 0.25 \times 10^{-2} \text{ m},$ and $A = 1.54 \times 10^{-4} \text{ m}^2$. The air density, bulk modulus, and mass of air in the exposed sections are $\rho =$ 1.21 kg m⁻³, $B = 1.42 \times 10^5$ Pa, and $M = 1.21 \times 10^{-7}$ kg, respectively. In Fig. 2(a), we notice that the lower boundary at kL = 0 does not shift, indicating that the first cutoff frequency is independent of the modulation speed. This is because the first cutoff frequency

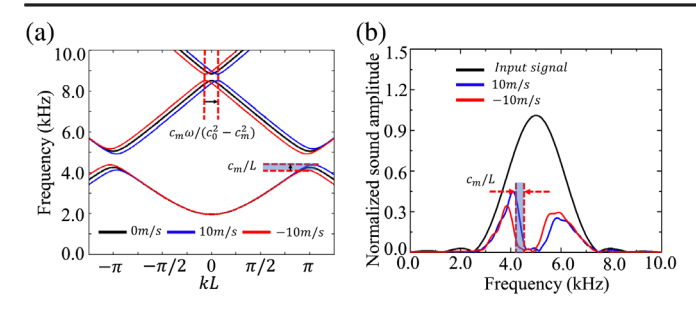


FIG. 2. (a) Analytically calculated dispersion diagrams of the modulated effective medium with $c_m=10$ (solid blue), 0 (solid black), and -10 m/s (solid red). A frequency shift of the band gap lower bound $\Delta f=c_m/L$ is obtained when modulated from $c_m=10$ to $c_m=-10$ m/s. (b) Normalized sound amplitudes from numerical simulations for modulation speeds $c_m=10$ (solid blue) and $c_m=-10$ m/s (solid red). The solid black curve represents the input signal.

corresponds to a stationary wave at k = 0 and therefore is insensitive to the modulation when the modulation speed is slow. The effect of the modulation speed on the cutoff frequency has been investigated in detail [43]. However, its upper boundary exhibits a frequency shift of c_m/L . Accordingly, the band gaps become directional, resulting in nonreciprocal wave propagation at these frequencies. Frequency shifts of the second and third passbands are also observed. The continuous modulation-induced tilting of the dispersion curves can be interpreted by the adiabatic theorem for slow modulation. The frequency shift is determined by $C\omega_m$, where C is the Chern number (Supplemental Material [42], Sec. B). To validate the theoretical prediction, numerical simulations for the modulated system (Fig. 1) are conducted using a finite-element method (FEM)-based software COMSOL Multiphysics. In the simulations, a five-cycle tone burst signal $p = [1 - \cos(0.5\pi f_c t)] \sin(2\pi f_c t)$ centered at $f_c =$ 5 kHz is applied at one end of the tube and the timedomain transmitted signal is measured at the other end. Based on Fourier transform, Fig. 2(b) illustrates the frequency spectra of the incidence and transmission with $c_m = 10 \text{ m/s}$ and without modulation. To reduce the undesired reflection, time-domain perfect matching layers are applied on both ends of the tube (Supplemental Material [42], Sec. C). As shown in Fig. 2, the acoustic nonreciprocity is observed around the lower and upper boundaries of the first stop band, shifting the first branch up to c_m/L compared with the nonmodulated case. A possible realistic experimental setup and the associated measuring procedure are discussed in Sec. C of the Supplemental Material [42]. In addition, the acoustic wave propagation at other frequencies are tilted with transmitted amplitudes unaltered. The time-domain numerical results demonstrate that the acoustic pumping is sufficient to break reciprocity when traveling along the modulation direction and suppressed in the other direction.

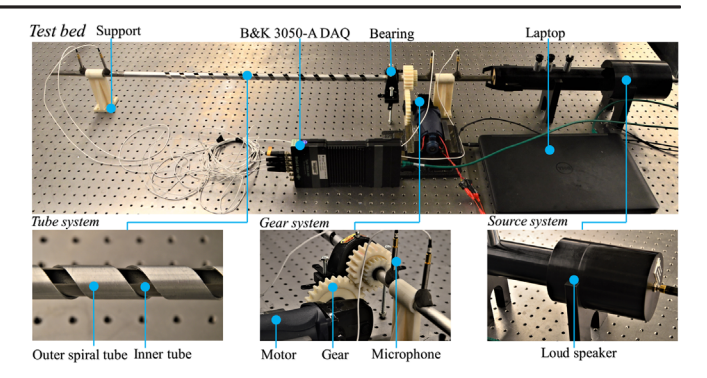


FIG. 3. Experimental setup of the spatiotemporal modulated acoustic system. The test bed is composed of three main components: a tube system composed of the slotted tube and exposed helical tube, a gear system and motor to drive the rotation of the outer helical tube, and an acoustic testing system containing a loudspeaker and four acoustic transducers (probes).

We experimentally demonstrate the acoustic bandtilting-induced nonreciprocity using a purely mechanical test bed, as shown in Fig. 3. The test bed, fixed to a vibration isolation platform by 3D printed supports, is a full realization of the numerical model illustrated in Fig. 1. Both the slotted and helical tubes are made from aluminum. The inner slotted tube and outer helical tube have inner radii of 7 and 8.2 mm and outer radii of 8 and 9.3 mm, respectively. The helical tube is rotated by a motor. We used Mecanum's four microphone impedance tubes and collected the data with a B&K 3050-A data acquisition (DAQ) system. While the helical tube rotates, the ESs translate along the tube axis (see video in the Supplemental Material [42]). Acoustic signals are generated with a loudspeaker on the right side of the tube. Four acoustic transducers, working as probes, are placed to collect the reflected and transmitted signals (see Fig. 3). The contact areas of the two tubes are filled with lubricant to prevent sound leakage and reduce noise.

We first measured the sound transmission by translating the ESs characterized by moving boundary conditions. The loudspeaker is driven a by swept-sine input covering 1–5 kHz. When the rotation is sufficiently slow to satisfy the adiabatic condition, the bulk bands of the modulated tube are tilted with respect to their static reference configuration (see also Fig. 2). A directional band gap appears around 4450 Hz with a small modulation speed of $c_m = +10$ m/s. This enables the sound to transmit within the frequency range of $4450-(4450+c_m/2L)$ Hz, which is forbidden when the tube is static. In other words, nonreciprocal sound transport is triggered within the band gap when the tube is rotating; see Fig. 4(a). As expected, good agreement between numerical and experimental results is observed. The nonreciprocal frequency region is marked by the blue-shaded area in Fig. 4(a), where the clockwise (CW) and counterclockwise (CCW) modulations display asymmetric transmission with a bandwidth of

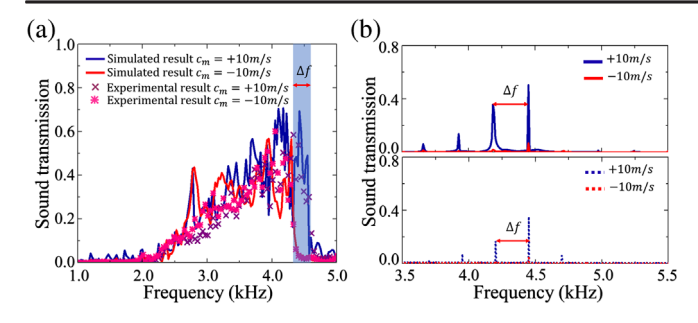


FIG. 4. Comparison of the sound transmission spectrum of the spatiotemporally modulated acoustic material. (a) Simulation results with modulation speeds $c_m=10$ (solid blue) and $c_m=-10$ m/s (solid red), and the corresponding experimental results with modulation speeds $c_m=10$ (purple cross) and $c_m=-10$ m/s (pink star). (b) Simulations (solid) and experiments (dotted) for modulation speeds $c_m=10$ (blue) and $c_m=-10$ m/s (red) under the excitation at 4450 Hz.

 $\Delta f = c_m/L$. To better quantify the nonreciprocal behavior, numerically and experimentally attained transmission spectra under harmonic loading at $f_e = 4450$ Hz is plotted in Fig. 4(b). The magnitudes of sound transmission at the excitation frequencies (within the modulation passband) are significantly greater than those for the negative modulation (within the modulation band gap). Moreover, the intensities of lower harmonics (in the passband) are much stronger than those of the higher ones (within the band gap). Further, high-order harmonics are observed as additional peaks, with multiple frequencies $f = f_e \pm n\Delta f$, where $\Delta f = 250$ Hz, and n = 0, 1, 2, ... These extra harmonics are the consequence of the traveling waves being scattered by the moving boundaries as in the Doppler effect [6]. It should be mentioned that, in spite of the lossy characteristics of the ESs, the nonreciprocal behavior is still noticeable since it is quantized by a robust Chern number (Supplemental Material [42], Secs. B and C).

Topological pumping and band-tilting-induced nonreciprocity in our system have an identical underlying origin: both are characterized by the same Chern number. To examine the topological pumping, it is essential to quantify the acoustic mode shapes through a pumping cycle: it overcomes (or overrides) the band gap and enables the propagation of sound within it and, further, can be captured by a nonzero Chern number according to the principle of bulk-edge correspondence [46]. In the current design, we can assume that the CW rotation of the tube corresponds to the modulation of the ESs in the forward direction (0–20 mm). In this way, the CCW rotation automatically corresponds to the backward modulation (20-0 mm). Figure 5(a) shows the numerically calculated eigenfrequencies of a finite tube composed of 15 ESs with different edge position instants under fixed boundary conditions applied upon both ends (see Supplemental Material [42], Sec. C for more numerical details). As the helical tube rotates, the right and left edge modes, marked by the red and blue dots in Fig. 5(a), exist within the band gap. Within one modulation period, a transition from the bulk mode, to the right edge, then back to the bulk, and eventually to the left mode can be identified, exhibiting the adiabatic topological pumping process. The mode shapes of the (i) bulk mode, (ii) right edge mode, and (iii) left edge mode are correspondingly shown in Fig. 5(b) for demonstration purposes.

To observe the topological pumping, we conduct experiments by turning the tube under different boundary conditions to examine the bulk-edge correspondence principle through a pumping cycle (Supplemental Material [42], Sec. D). The test bed is identical to what has been shown in Fig. 3, except the helical tube is manually turned to certain position instants and remains static. A microphone with subwavelength dimension is placed inside the tube for scanning the pressure field distribution along the tube axis (Supplemental Material [42], Sec. D). Harmonic excitations of different frequencies are then applied when the phase of the modulated tube is swept over one complete rotation of 2π by manually translating the ESs from 0 to 20 mm (Supplemental Material [42], Sec. D). The measured pressure field distributions at three different position instants, corresponding to the three highlighted eigenmodes in Fig. 5(a), are presented in Fig. 5(b) by symbol plots. For the bulk mode around 4.4 kHz illustrated in Fig. 5(b)(i), except for the magnitude decrease due to sound attenuation, a standing wave profile is still observable describing the bulk mode. The right (under the left excitation) and left (under the right excitation) edge modes are shown in Fig. 5(b)(ii) and (iii), respectively. The establishment of the acoustic localization under the excitations on the opposite sides proves the existence of the

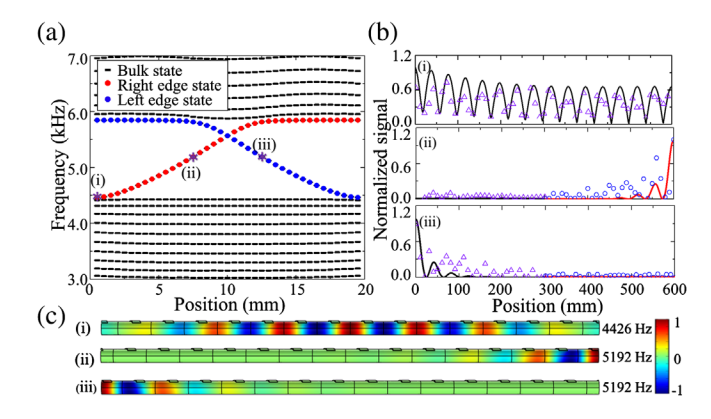


FIG. 5. (a) Evolution of eigenfrequencies of a finite tube (15 unit cells) over one period of modulation under fixed boundary condition. (b) Normalized acoustic pressure distributions at modes (i)–(iii) shown in (a). The black and red solid curves denote the simulation incident signals from the right and left sides, respectively. The purple triangular and blue circular dots represent the corresponding experimental measurements. (c) Mode shapes (pressure distribution) from FEM numerical simulations at modes (i)–(iii).

topological edge modes (Supplemental Material [42], Sec. D). Eigenfrequency analysis also provides the acoustic pressure distributions at these position instants (i)–(iii), as shown in Fig. 5(c). Good agreement with the measured normalized acoustic distributions is evidenced. Finally, to directly validate the localized edge mode, broadband acoustic harmonic tests are implemented by applying acoustic excitation on both the right and left sides of the system under phase condition (ii) (see Supplemental Material [42], Sec. D for the measured frequency spectrum of the edge mode). The results confirm the emergence of the topologically protected edge mode localized around the right end of the tube under the current phase condition.

In summary, we have experimentally demonstrated the mechanically modulation-induced nonreciprocity in acoustics and the adiabatic topological pumping phenomena, associated with the purely mechanical realization of spatiotemporally modulated acoustic waveguide. The spatiotemporal modulation behaving as an acoustic pumping strategy offers unprecedented control and reconfigurability over the acoustic energy transport in space and even in frequency dimensions. We believe that the proposed mechanical realization of the acoustic modulated nonreciprocal systems paves the way for realizing topological phononic logic and acoustic energy localization and trapping applications.

This work is supported by the Air Force Office of Scientific Research under Grants No. AF 9550-18-1-0342 and No. AF 9550-20-0279, the NSF EFRI under Grant No. 1641078, and the Army Research Office under Grant No. W911NF-18-1-0031.

- X. X., Q. W. and H. C. contributed equally to this work. huangg@missouri.edu
- [1] R. Fleury, D. L. Sounas, C. F. Sieck, M. R. Haberman, and A. Alù, Science 343, 516 (2014).
- [2] N. Boechler, G. Theocharis, and C. Daraio, Nat. Mater. 10, 665 (2011).
- [3] S. Zhang, L. Yin, and N. Fang, Phys. Rev. Lett. **102**, 194301 (2009).
- [4] J. Zhu, J. Christensen, J. Jung, L. Martin-Moreno, X. Yin, L. Fok, X. Zhang, and F. J. Garcia-Vidal, Nat. Phys. 7, 52 (2011).
- [5] T. Brunet, A. Merlin, B. Mascaro, K. Zimny, J. Leng, O. Poncelet, C. Aristégui, and O. Mondain-Monval, Nat. Mater. 14, 384 (2015).
- [6] B. Liang, X. S. Guo, J. Tu, D. Zhang, and J. C. Cheng, Nat. Mater. 9, 989 (2010).
- [7] H. Nassar, H. Chen, A. N. Norris, and G. L. Huang, Phys. Rev. B 97, 014305 (2018).
- [8] H. Nassar, B. Yousefzadeh, R. Fleury, M. Ruzzene, A. Alù, C. Daraio, A. N. Norris, G. Huang, and M. R. Haberman, Nat. Rev. Mater. 5, 667 (2020).
- [9] D. Jalas, A. Petrov, M. Eich, W. Freude, S. Fan, Z. Yu, R. Baets, M. Popović, A. Melloni, J. D. Joannopoulos, and M. Vanwolleghem, Nat. Photonics 7, 579 (2013).

- [10] L. Lin, P. Hu, J. Shi, C. M. Appleton, K. Maslov, L. Li, R. Zhang, and L. V. Wang, Nat. Commun. 9, 2352 (2018).
- [11] H. S. Park and B. K. Oh, J. Sound Vib. 418, 122 (2018).
- [12] J. W. Strutt, Proc. London Math. Soc. s1-4, 357 (1871).
- [13] J. A. Achenbach and J. D. Achenbach, *Reciprocity in Elastodynamics* (Cambridge University Press, Cambridge, England, 2003).
- [14] M. R. Haberman and M. D. Guild, Phys. Today **69**, No. 6, 42 (2016).
- [15] S. A. Cummer, J. Christensen, and A. Alù, Nat. Rev. Mater. 1, 16001 (2016).
- [16] Y. Zheng, Z. Wu, X. Zhang, and K. W. Wang, Smart Mater. Struct. **28**, 045005 (2019).
- [17] B. Yuan, B. Liang, J. C. Tao, X. Y. Zou, and J. C. Cheng, Appl. Phys. Lett. **101**, 043503 (2012).
- [18] A. B. Khanikaev, S. H. Mousavi, W. K. Tse, M. Kargarian, A. H. MacDonald, and G. Shvets, Nat. Mater. 12, 233 (2013).
- [19] Z. Zhang, Q. Wei, Y. Cheng, T. Zhang, D. Wu, and X. Liu, Phys. Rev. Lett. 118, 084303 (2017).
- [20] L. M. Nash, D. Kleckner, A. Read, V. Vitelli, A. M. Turner, and W. T. Irvine, Proc. Natl. Acad. Sci. U.S.A. 112, 14495 (2015).
- [21] D. J. Apigo, W. Cheng, K. F. Dobiszewski, E. Prodan, and C. Prodan, Phys. Rev. Lett. 122, 095501 (2019).
- [22] M. Maldovan. Nature (London) 503, 209 (2013).
- [23] C. Liu, Z. Du, Z. Sun, H. Gao, and X. Guo, Phys. Rev. Applied 3, 064014 (2015).
- [24] Z. Zhang, I. Koroleva, L. I. Manevitch, L. A. Bergman, and A. F. Vakakis, Phys. Rev. E 94, 032214 (2016).
- [25] B. I. Popa and S. A. Cummer, Nat. Commun. 5, 3398 (2014).
- [26] B. Liang, B. Yuan, and J. C. Cheng, Phys. Rev. Lett. **103**, 104301 (2009).
- [27] P. Wang, L. Lu, and K. Bertoldi, Phys. Rev. Lett. 115, 104302 (2015).
- [28] M. Garau, M. J. Nieves, G. Carta, and M. Brun, Int. J. Eng. Sci. 143, 115 (2019).
- [29] R. Fleury, D. L. Sounas, and A. Alù, Phys. Rev. B 91, 174306 (2015).
- [30] Y. G. Peng, C. Z. Qin, D. G. Zhao, Y. X. Shen, X. Y. Xu, M. Bao, H. Jia, and X. F. Zhu, Nat. Commun. 7, 13368 (2016).
- [31] Y. Wang, B. Yousefzadeh, H. Chen, H. Nassar, G. Huang, and C. Daraio, Phys. Rev. Lett. **121**, 194301 (2018).
- [32] Y. Chen, X. Li, H. Nassar, A. N. Norris, C. Daraio, and G. Huang, Phys. Rev. Applied 11, 064052 (2019).
- [33] C. Shen, X. Zhu, J. Li, and S. A. Cummer, Phys. Rev. B 100, 054302 (2019).
- [34] J. Li, C. Shen, X. Zhu, Y. Xie, and S. A. Cummer, Phys. Rev. B 99, 144311 (2019).
- [35] A. Baz, J. Acoust. Soc. Am. 143, 1376 (2018).
- [36] S. P. Wallen and M. R. Haberman, Phys. Rev. E 99, 013001 (2019).
- [37] B. M. Goldsberry, S. P. Wallen, and M. R. Haberman, J. Acoust. Soc. Am. 146, 782 (2019).
- [38] I. H. Grinberg, M. Lin, C. Harris, W. A. Benalcazar, C. W. Peterson, T. L. Hughes, and G. Bahl. Nat. Commun. 11, 974 (2020).
- [39] Q. Wu, H. Chen, H. Nassar, and G. L. Huang, J. Mech. Phys. Solids 146, 104196 (2020).

- [40] A. A. Oliner and A. Hessel, IEEE Trans. Microwave Theory Tech 9, 337 (1961).
- [41] S. H. Lee, C. M. Park, Y. M. Seo, Z. G. Wang, and C. K. Kim, J. Phys. Condens. Matter **21**, 175704 (2009).
- [42] See Supplemental Material at http://link.aps.org/supplemental/ 10.1103/PhysRevLett.125.253901 for more details on analytical modeling of the modulated acoustic tube with exposed sections, topological pumping and Chern number, and simulation and experimental methods, which includes Refs. [7,41,43,44].
- [43] H. Nassar, X. C. Xu, A. N. Norris, and G. L. Huang, J. Mech. Phys. Solids 101, 10 (2017).
- [44] T. Fukui, Y. Hatsugai, and H. Suzuki, J. Phys. Soc. Jpn. **74**, 1674 (2005).
- [45] G. M. Gibson, E. Toninelli, S. A. Horsley, G. C. Spalding, E. Hendry, D. B. Phillips, and M. J. Padgett, Proc. Natl. Acad. Sci. U.S.A. 115, 3800 (2018).
- [46] H. Chen, L. Y. Yao, H. Nassar, and G. L. Huang, Phys. Rev. Appl. **11**, 044029 (2019).

Physical observation of a robust acoustic pumping in waveguides with dynamic boundary: supplementary material

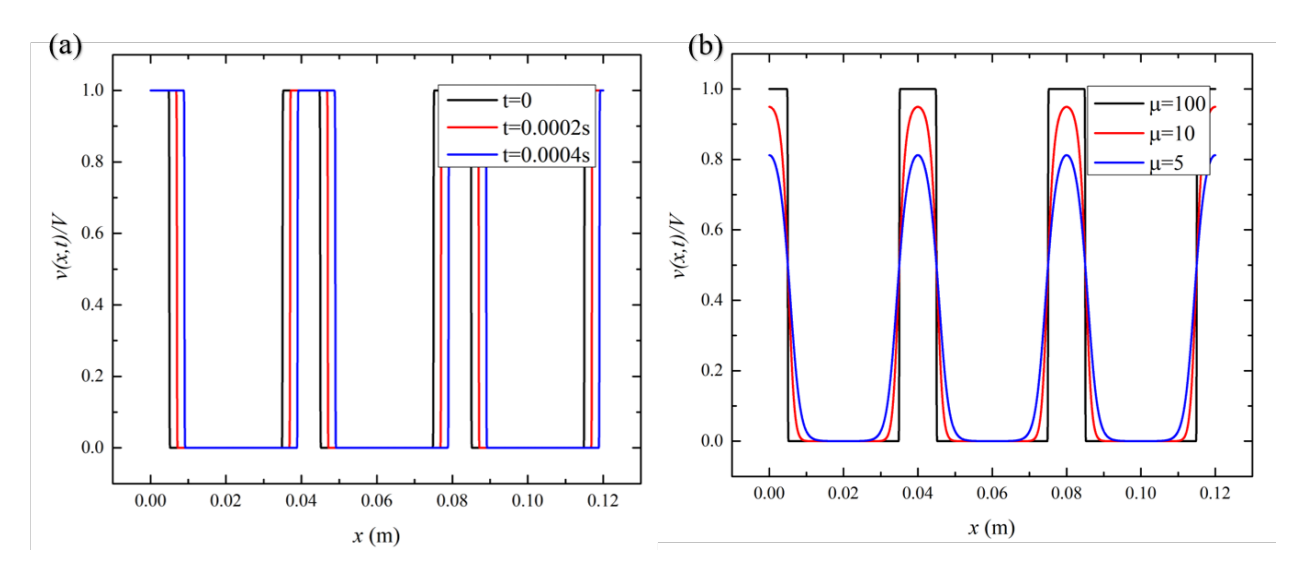
Xianchen Xu,^{1†} Qian Wu,^{1†} Hui Chen,^{1†} Hussein Nassar,¹ Yangyang Chen,¹ Andrew Norris,²
Michael R. Haberman³ and Guoliang Huang^{1*}

Section A: ANALYTICAL MODELING OF THE MODULATED ACOUSTIC TUBE WITH EXPOSED SECTIONS

In the modulated system, the transition of the boundary condition in the tube is quite abrupt as the vertical velocity goes from zero to nonzero almost instantaneously, which is shown in Fig. S1(a). In the simulations, to improve numerical convergence, the transition of the boundary conditions needs to be smoothed out. For the purpose, the original square wave function has been mathematically represented by a logistic function to describe the boundary condition and vertical velocity. As the exposed section moves at the modulation speed c_m , the modulated vertical velocity in each unit cell can hence be expressed by using the logistic function as

$$v(x,t) = V\{1 + \exp\left[-\mu\cos(\omega_m t - k_m x) - \mu\cos(\pi y)\right]\}^{-1}$$
 (S1)

where μ denotes the logistic growth rate, V is the amplitude of vertical velocity at the exposed sections, $L = L_1 + L_2$ represents the unit cell size, $\gamma = \frac{L_2}{L}$, $\omega_m = k_m c_m$ and $k_m = \frac{2\pi}{L}$.



[†]Author contributed equally

¹ Department of Mechanical and Aerospace Engineering, University of Missouri, Columbia, MO 65211, USA
² Mechanical and Aerospace Engineering, Rutgers University, Piscataway, NJ 08854-8058, USA
³ Walker Department of Mechanical Engineering and Applied Research Laboratories, The University of Texas at Austin, Austin, TX 78712, USA.

^{*}Email:huangg@missouri.edu

FIG. S1. (a) Normalized vertical velocity at the boundaries of the exposed sections with $\mu = 100$ and t = 0 s, 0.0002 s, and 0.0004 s. (b) Normalized vertical velocity described by the logistic function at t = 0 with grow rate being $\mu = 5$, 10, and 100.

Fig. R1(b) illustrates the vertical velocity described by the logistic function. In the numerical simulation, the growth rate $\mu = 5$ is chosed to make trade-off between equivalently realizing square wave function and facilitating the numerical convergence. Actually, due to the significant impedance mismatch, $\mu = 5$, 10, or 100 does not make difference in numerical results.

The equilibrium equation for the air in the ES can be formulated as:

$$p(x,t)S = M\partial_t v(x,t), \tag{S2}$$

where M is mass of air of the ES with $M = \rho Sh$, h is the height of the ES. Then the governing equations for the homogenized tube at the ES are written as [1]:

$$-\left(\frac{1}{B}\right)\partial_t p(x,t) = \partial_x u(x,t) + \left(\frac{\sigma_1}{A}\right)v(x,t),\tag{S3}$$

$$-\partial_x p(x,t) = \rho \partial_t u(x,t), \tag{S4}$$

where B and ρ are the bulk modulus and density of the air in the tube, A denotes the cross-section area of the tube, $\sigma_1 = NS$ with $N = (L_1 + L_2)^{-1}$, where S denote the cross-sectional area of the ES. Differentiating the equation (S3) with respect to t and the equation (S4) with respect to x lead to

$$\partial_t \left[-\left(\frac{1}{B}\right) \partial_t p(x,t) \right] = \partial_t \left[\partial_x u(x,t) + \left(\frac{\sigma_1}{A}\right) v(x,t) \right], \tag{S5}$$

$$-\partial_x^2 p(x,t) = \rho \partial_x [\partial_t u(x,t)], \tag{S6}$$

Ignoring the loss for simplicity, substituting the equations (S2) and (S6) into (S5) simplifies to

$$-\left(\frac{1}{B}\right)\partial_t^2 p(x,t) = -\frac{1}{\rho}\partial_x^2 p(x,t) + \left(\frac{\sigma_1}{A}\frac{S}{M}\right)p(x,t),\tag{S7}$$

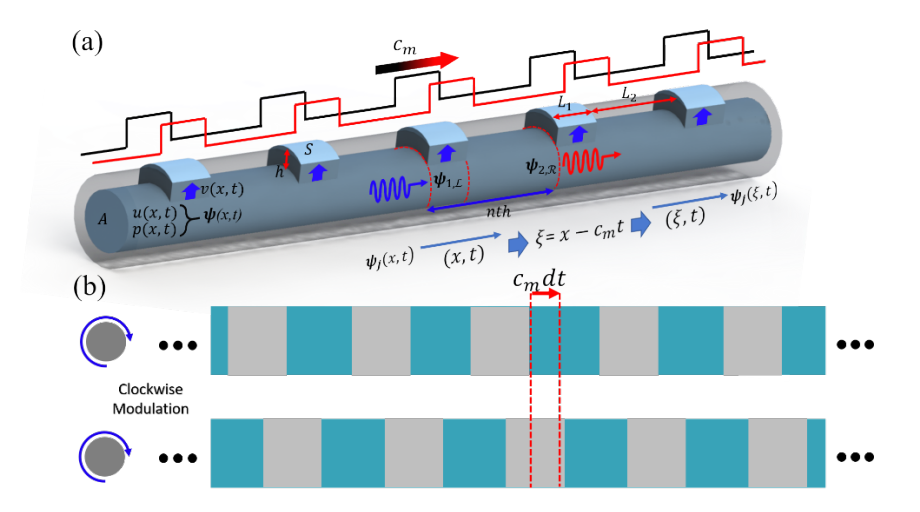


FIG. S2. (a) Section view of the experimental setup with the unit cell boxed by dashed lines. (b) Effective 1D modulated metamaterial under the clockwise spinning of the outer tube.

From another point of view, as shown in Fig. S2(b), the tube can be regarded as a 1D phononic crystal. In addition, by spinning the outer tube counterclockwise (clockwise), the ES "travel" along the positive (negative) direction as Fig. S2(b). It should be noted that, by spinning the outer tube, i.e., under the proposed spatiotemporal modulations, a bias is introduced in space and time and breaks time-reversal symmetry: in general, if the acoustic medium supports a wave u(x, t), it will not support u(-x, t).

Specifically, for the case the ES "traveling" with a certain speed c_m , the tube with the exposed and covered parts will be modulated with the speed c_m . By introducing a new variable $\xi = x - c_m t$, the equation (S7) can be rewritten as

$$-\left(\frac{1}{B}\right)\left(\partial_{t}-c_{m}\,\partial_{\xi}\right)^{2}p(\xi,t) = -\frac{1}{\rho}\,\partial_{\xi}^{2}p(\xi,t) + \left(\frac{\sigma_{\text{SH}}\,S}{A\,M}\right)p(\xi,t),\tag{S8}$$

The governing equations in these two mediums with exposed and covered parts can be expressed as two different types.

Medium 1: At $nL < \xi < L_1 + nL$

$$-\left(\frac{1}{B}\right)\left(\partial_{t}-c_{m}\,\partial_{\xi}\right)^{2}p_{1}(\xi,t)=-\frac{1}{\rho}\,\partial_{\xi}^{2}p_{1}(\xi,t)+\left(\frac{\sigma_{1}}{A}\frac{S}{M}\right)p_{1}(\xi,t),\tag{S9}$$

Medium 2: At $L_1 + nL < \xi < L_1 + L_2 + nL$

$$-\left(\frac{1}{B}\right)\left(\partial_t - c_m \,\partial_\xi\right)^2 p_2(\xi, t) = -\frac{1}{\rho} \,\partial_\xi^2 p_2(\xi, t) \,, \tag{S10}$$

[Type here]

Let phase velocity $c_0 = \sqrt{B/\rho}$, $c_h = \sqrt{B/M}$, where c_0 is the original sound speed in the air, and c_h is the effective sound speed influenced by the ES. Note that with cover on the tube, the equation (S9) will be reduced to equation (S10), and these two mediums will be the same, otherwise, these two mediums will be different. We begin by deriving the dispersion relation for media with unit cells of arbitrary profiles, and then move on to consider applications to laminates composed of discrete phases.

We assume the pressure solutions of the tube with exposed and covered parts are

$$p_1(\xi, t) = A_1 e^{ik_1 \xi} e^{-i\Omega t}, p_2(\xi, t) = A_2 e^{ik_2 \xi} e^{-i\Omega t} , \qquad (S11)$$

where k_1 and k_2 are the wavenumbers in the tube with exposed and covered parts respectively, A_1 and A_2 are the amplitudes of the acoustic pressure in the tube with exposed and covered parts respectively. In the following, we will use subscript 1 and 2 in the letters to represent the variables for tube with exposed and covered parts respectively.

Substituting the equation (S11) into (S9) and (S10), we have

$$k_1 = \frac{c_m \Omega \pm \sqrt{c_0^2 \Omega^2 + c_m^2 \eta c_h^2 - c_0^2 \eta c_h^2}}{c_0^2 - c_m^2}, k_2 = \frac{c_m \Omega \pm \sqrt{c_0^2 \Omega^2}}{c_0^2 - c_m^2} = \frac{c_m \Omega \pm c_0 \Omega}{c_0^2 - c_m^2},$$

Specifically, for the case wave propagates along the positive direction,

$$k_{1+} = \frac{c_m \Omega + \sqrt{c_0^2 \Omega^2 + c_m^2 \eta c_h^2 - c_0^2 \eta c_h^2}}{c_0^2 - c_m^2}, \ k_{2+} = \frac{c_m \Omega + c_0 \Omega}{c_0^2 - c_m^2} = \frac{\Omega}{c_0 - c_m},$$

while for the case wave propagates along the negative direction,

$$k_{1-} = \frac{c_m \Omega - \sqrt{c_0^2 \Omega^2 + c_m^2 \eta c_h^2 - c_0^2 \eta c_h^2}}{c_0^2 - c_m^2}, \ k_{2-} = \frac{c_m \Omega - c_0 \Omega}{c_0^2 - c_m^2} = -\frac{\Omega}{c_0 + c_m},$$

Here, index (\pm) indicates wave propagation direction positive or negative. Notably, there exists a nontrivial relation between the wavenumbers along with the two directions

$$k_{1+} + k_{1-} = k_{2+} + k_{2-} = \frac{c_m \Omega}{c_0^2 - c_m^2}$$

which indicates that under the modulation the wave propagation in two mediums is unsymmetrical. While for the symmetrical wave propagation, the wavenumber between two directions should have a trivial relation:

$$k_{1+} + k_{1-} = k_{2+} + k_{2-} = 0,$$

The pressure and vertical velocity fields in the tube with exposed and covered parts can be formulated into the following forms:

$$p_{1}(\xi,t) = A_{1+}e^{-ik_{1+}\xi}e^{-i\Omega t} + A_{1-}e^{-ik_{1-}\xi}e^{-i\Omega t},$$

$$p_{2}(\xi,t) = A_{2+}e^{-ik_{2+}\xi}e^{-i\Omega t} + A_{2-}e^{-ik_{2-}\xi}e^{-i\Omega t},$$
(S12)

Thus, we assume the vertical velocity in tube with exposed and covered parts also have similar forms, expressed as:

$$u_{1}(\xi,t) = B_{1+}e^{-ik_{1+}\xi}e^{-i\Omega t} + B_{1-}e^{-ik_{1-}\xi}e^{-i\Omega t},$$

$$u_{2}(\xi,t) = B_{2+}e^{-ik_{2+}\xi}e^{-i\Omega t} + B_{2-}e^{-ik_{2-}\xi}e^{-i\Omega t}$$
(S13)

According to the equilibrium equations in the tube with exposed and covered parts, i.e.,

$$-\frac{1}{\rho}\partial_{\xi}p_{1}(\xi,t) = -c_{m}\,\partial_{\xi}u_{1}(\xi,t) + \partial_{t}u_{1}(\xi,t), \text{ and}$$

$$-\frac{1}{\rho}\partial_{\xi}p_{2}(\xi,t) = -c_{m}\,\partial_{\xi}u_{2}(\xi,t) + \partial_{t}u_{2}(\xi,t), \tag{S14}$$

the relation between the amplitude, wavenumber, and frequency can be expressed as

$$B_{1+} = \frac{k_{1+}}{\rho(c_m k_{1+} - \Omega)} A_{1+} = b_{1+} A_{1+},$$

$$B_{1-} = \frac{k_{1-}}{\rho(c_m k_{1-} - \Omega)} A_{1-} = b_{1-} A_{1-},$$

with
$$b_{1+} = \frac{k_{1+}}{\rho(c_m k_{1+} - \Omega)}$$
 and $b_{1-} = \frac{k_{1-}}{\rho(c_m k_{1-} - \Omega)}$.

At the left interface of tube with the ES, the pressure and vertical velocity can be rewritten as:

$${p_{1,\mathcal{L}} \brace u_{1,\mathcal{L}}} = \begin{bmatrix} 1 & 1 \\ b_{1+} & b_{1-} \end{bmatrix} {A_{1+} \brace A_{1-}},$$
 (S15)

" \mathcal{R} " and " \mathcal{L} " indicate the acoustic field at right and left of interface of tube with exposed and covered parts respectively. Correspondingly, at the right interface of tube with the ES, the pressure and vertical velocity can be rewritten as:

$${A_{1+} \atop A_{1-}} = \frac{1}{b_{1+}-b_{1-}} \begin{bmatrix} -b_{1-}e^{ik_{1+}L_{1}} & e^{ik_{1+}L_{1}} \\ b_{1+}e^{ik_{1-}L_{1}} & -e^{ik_{1-}L_{1}} \end{bmatrix} {p_{1,\mathcal{R}} \atop u_{1,\mathcal{R}}},$$
(S16)

Note that the pressure and vertical velocity at both boundaries of tube with the ES has the following relation:

$${p_{1,\mathcal{L}} \brace u_{1,\mathcal{L}}} = \frac{1}{b_{1+}-b_{1-}} \begin{bmatrix} -b_{1-}e^{ik_{1+}L_{1}} + b_{1+}e^{ik_{1-}L_{1}} & e^{ik_{1+}L_{1}} - e^{ik_{1-}L_{1}} \\ -b_{1+}b_{1-}(e^{ik_{1+}L_{1}} - e^{ik_{1-}L_{1}}) & b_{1+}e^{ik_{1+}L_{1}} - b_{1-}e^{ik_{1-}L_{1}} \end{bmatrix} {p_{1,\mathcal{R}} \brace u_{1,\mathcal{R}}}, (S17)$$

A similar relation holds for tube with covered part as:

$${p_{2,\mathcal{L}} \atop u_{2,\mathcal{L}}} = \frac{1}{b_{2+} - b_{2-}} \begin{bmatrix} -b_{2-} e^{ik_{2+}L_2} + b_{1+} e^{ik_{2-}L_2} & e^{ik_{2+}L_2} - e^{ik_{2-}L_2} \\ -b_{2+} b_{2-} (e^{ik_{2+}L_1} - e^{ik_{2-}L_1}) & b_{2+} e^{ik_{2+}L_2} - b_{2-} e^{ik_{2-}L_2} \end{bmatrix} {p_{2,\mathcal{R}} \atop u_{2,\mathcal{R}}}, \quad (S18)$$

with
$$b_{2+} = \frac{k_{2+}}{\rho(c_m k_{2+} - \Omega)}$$
 and $b_{2-} = \frac{k_{2-}}{\rho(c_m k_{2-} - \Omega)}$.

Therefore the transfer matrices between tube with exposed and covered parts can be expressed as:

$$\mathbf{T}_{1} = \frac{1}{b_{1+}-b_{1-}} \begin{bmatrix} -b_{1-}e^{ik_{1+}L_{1}} + b_{1,t}e^{ik_{1-}L_{1}} & e^{ik_{1+}L_{1}} - e^{ik_{1-}L_{1}} \\ -b_{1+}b_{1-}(e^{ik_{1+}L_{1}} - e^{ik_{1-}L_{1}}) & b_{1+}e^{ik_{1+}L_{1}} - b_{1-}e^{ik_{1-}L_{1}} \end{bmatrix}$$
(S19)

$$\mathbf{T}_{2} = \frac{1}{b_{2+} - b_{2-}} \begin{bmatrix} -b_{2-} e^{ik_{2} + L_{2}} + b_{1,t} e^{ik_{2} - L_{2}} & e^{ik_{2} + L_{2}} - e^{ik_{2} - L_{2}} \\ -b_{2+} b_{2-} (e^{ik_{2} + L_{1}} - e^{ik_{2} - L_{1}}) & b_{2+} e^{ik_{2} + L_{2}} - b_{2-} e^{ik_{2} - L_{2}} \end{bmatrix}$$
(S20)

For simplification, the pressure and vertical velocity in *n*th tube with exposed and covered parts are organized as a state vector:

$$\psi_j(\xi, t) = \{p_j(\xi, t), u_j(\xi, t)\}^{\mathrm{T}}, j = 1,2$$
 (S21)

Thus, the pressure and vertical velocity continue condition at the interface between tube with exposed and covered parts should satisfy as $\psi_{1,\mathcal{R}}(\xi,t) = \psi_{2,\mathcal{L}}(\xi,t)$, and $\psi_{2,\mathcal{R}}(\xi,t) = \psi_{1,\mathcal{L}}(\xi+L,t)$ Meanwhile, the acoustic field in tube with exposed and covered parts can be obtained by using transfer matrix method as as $\psi_{1,\mathcal{L}}(\xi,t) = T_1\psi_{1,\mathcal{R}}(\xi,t)$, and $\psi_{2,\mathcal{L}}(\xi,t) = T_2\psi_{2,\mathcal{R}}(\xi,t)$.

Note that the Equation (S21) implies that the pressure and vertical velocity are continuous across interfaces. In this manner, the transfer equation can be expressed as

$$\psi_{1,\mathcal{L}}(\xi,t) = T_1 T_2 \psi_{1,\mathcal{L}}(\xi + L,t)$$
 (S22)

subject to the Floquet-Bloch periodic boundary condition

$$\psi_{1,\mathcal{L}}(\xi,t) = e^{i\kappa(L_1 + L_2)} \psi_{1,\mathcal{L}}(\xi + L,t)$$
 (S23)

where wavenumber κ and frequency Ω describes the phase of the traveling wave in the moving frame of reference (ξ, t) . The existence of a non-trivial solution ψ satisfying the Floquet–Bloch boundary condition (S23) is therefore equivalent to the vanishing of the determinant

$$\det |\boldsymbol{T}_1 \boldsymbol{T}_2 - \boldsymbol{I} e^{i\kappa(L_1 + L_2)}| = 0 \tag{S24}$$

In the original frame (x,t), the traveling wavenumber κ and temporal frequency ω can be retrieved based on

$$kx - \omega t = \kappa \xi - \Omega t$$

From which it can be inferred that

$$k = \kappa$$
, $\Omega = \omega - c_m k$

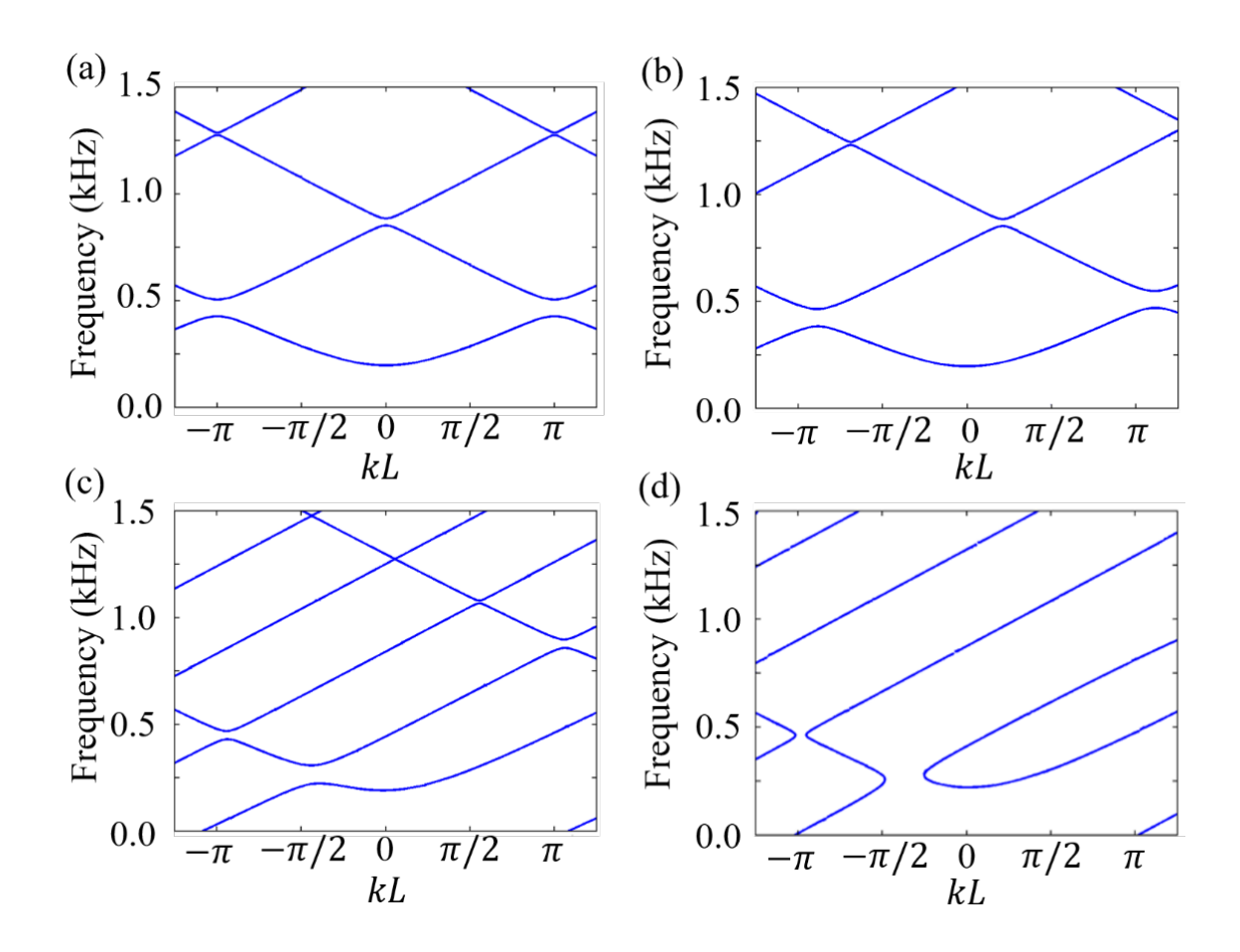


FIG. S3. schematically theoretical dispersion diagram of the modulated effective mediums with modulating speed: (a) $c_m = 0$, (b) $c_m = 0.1c_0$, (c) $c_m = 0.5c_0$, (d) $c_m = 1.5c_0$, respectively. Here, $c_0 = 343$ m/s is the sound velocity in air.

Here, the acoustic geometry parameters of the sonic crystal are $L_1 = 0.01$ m, $L_2 = 0.03$ m, $S = L_1^2 = 1 \times 10^{-4} \text{m}^2$, $\sigma_{SH} = 0.25 \times 10^{-2} \text{m}$, $A = 1.54 \times 10^{-4} \text{m}^2$, the material properties are $\rho = 1.21$ kg·m⁻³, $B = 1.42 \times 10^5$ Pa, $M = 1.21 \times 10^{-7}$ kg. From the eigenvalue equation (S24) we can get the theoretical dispersion relation in different modulation speeds. As shown in the Fig. S3 (a), with a modulation speed $c_m = 0$ the whole effective medium is a normal phononic crystal that follows the symmetry propagation law, and the dispersion relations are symmetrical in the Brillouin zone. As we discussed before, when the modulation is turned on, the symmetry will be broken. That is, as shown in the Fig. S3 (b), with the slow modulation speed $c_m = 0.1c_0$, the bandgap around 5 kHz before is the shift to higher frequency region for positive propagation and shift to lower frequency region for negation propagation, respectively. Hence, high-frequency bandgaps are the first to become directional whereas low-frequency bandgaps require higher

modulation speed. By fast modulations, i.e., the modulation speed c_m comparable to but lower than c_0 or greater than c_0 , for instance, with modulation speeds $c_m = 0.5c_0$ and $c_m = 1.5c_0$, the normal first bandgap has vanished as shown in Fig. S3 (c) and (d), while the wave propagation within such a phononic crystal is both dispersionless and reciprocal [2].

Section B. TOPOLOGICAL PUMPING AND CHERN NUMBER

For slow temporal modulations, slower than other characteristic time scales of the system, the topology of bulk bands fully dictates the band tilting and thus governs non-reciprocal transport. Therefore, the band tilting relates the nontrivial topology of a band to the non-reciprocal wave motion within the band. Other than band tilting, the topology of bulk bands suggests the existence of topological pumping in bulk gaps according to the principle of bulk-edge correspondence. Together, the band tilting and bulk-edge correspondence form a strong duo catering for the needs of robust one-way transmission. Guided by the theory, we perform experimental testing and fabricate a spatiotemporally modulated acoustic tube, where the proposed topological phenomena are achieved utilizing mechanical control to feature non-reciprocal transport (Fig. 2) and topological pumping (Fig. 5).

The appearance of band tilting and topological pumping caused by a slow modulation can be quantized [4], which relies on the evaluation of band's Chern number in the $(k, t) \in \mathbb{T}^2 = \left[-\frac{\pi}{L}, \frac{\pi}{L}\right] \times [0, T]$ space based on the adiabatic theorem and is given by

$$C = \frac{1}{2\pi i} \iint_{\mathcal{D}} \nabla \times Ad\mathcal{D},\tag{S25}$$

where $\mathcal{D} = \mathbb{T}^2$, $\nabla = (\partial/\partial k)e_k + (\partial/\partial t)e_t$, and $A = \psi^* \cdot \nabla \psi$, with ()* denoting a complex conjugate. The Chern number is evaluated numerically over a discretized (k,t) space according to the following procedures. Thanks to the adiabatic transform (modulation frequency here is taken much smaller than the width of bandgap), the continuous spatiotemporal evolution of eigenstates can be broken into a set of (k,t)-dependent snapshot eigenstates. In our work, (k,t) is discretized into a 301 × 301 grid. The corresponding eigenvector is defined as the complex pressure fields at evenly spaced points designated along the length of the unit cell. Here, 11 points are assigned, meaning that the eigenvector ψ at each (k,t) has 11 elements. At the (k_i,t_j) snapshot, where $i,j \in (1,301)$, the eigenvector $\psi_{i,j}$ is extracted. We then use the finite difference method to numerically calculate the Berry connection fields $(A_{i,j}^k, A_{i,j}^t)$, which can be obtained through

$$\mathbf{A}_{i,j}^{k} = Im\{\boldsymbol{\psi}_{i,j}^{*} \cdot \partial_{k} \boldsymbol{\psi}_{i,j}\}, \text{ with } \partial_{k} \boldsymbol{\psi}_{i,j} = \begin{cases} \frac{\boldsymbol{\psi}_{i,j} - \boldsymbol{\psi}_{i+1,j}}{\Delta k}, & i = 1\\ \frac{\boldsymbol{\psi}_{i+1,j} - \boldsymbol{\psi}_{i-1,j}}{2\Delta k}, & i \in [2,300]\\ \frac{\boldsymbol{\psi}_{i,j} - \boldsymbol{\psi}_{i-1,j}}{\Delta k}, & i = 301 \end{cases}$$

and

$$A_{i,j}^{t} = Im\{\psi_{i,j}^{*} \cdot \partial_{t}\psi_{i,j}\}, \text{ with } \partial_{t}\psi_{i,j} = \begin{cases} \frac{\psi_{i,j+1} - \psi_{i,j}}{\Delta t}, \ j = 1\\ \frac{\psi_{i,j+1} - \psi_{i,j-1}}{2\Delta t}, \ j \in [2,300]\\ \frac{\psi_{i,j} - \psi_{i,j-1}}{\Delta t}, \ j = 301 \end{cases}$$

where
$$\Delta k = \frac{1}{300} \frac{2\pi}{L}$$
 and $\Delta t = \frac{T}{300}$.

The Berry curvature is the curl of the Berry connection field, and can be calculated in a similar fashion

$$\mathbf{B} = \partial_k \mathbf{A}_{i,j}^t - \partial_t \mathbf{A}_{i,j}^k$$

The Berry curvature is then integrated over the entire Brillouin zone to obtain the Chern number. As a result, the Chern number of the first branch is +1 for the clockwise modulation ($c_m = 10 \text{ m/s}$), and -1 for the anticlockwise modulation ($c_m = -10 \text{ m/s}$). More precisely, the sign of Chern number determines the direction of tilting. Even more remarkably, the width of the one-way-transport frequency window is uniquely determined by the topological index, C, and by the modulation frequency, ω_m , as $C\omega_m$. Other than characterizing band tilting, the bulk-edge correspondence indicates that the number of edge modes equals the gap Chern number and the sign agrees with the direction of edge waves. Using this principle, one can immediately predict either the presence or absence of edge modes at a particular frequency.

Section C: SIMULATION METHOD

Modulation simulation

We use COMSOL Multiphysics to simulate the band-tilting induced non-reciprocity. The total length of the tube is 1600 mm, where the modulated structures are located in the middle of the tube. We send in the incident signal at one side and apply PML at both sides. For the modulated layer, the logistic function to realize the moving of the boundary as

$$\{c, \rho\} = \mathcal{L}(x, t) \cdot \{c_n, \rho_n\} \tag{S25}$$

$$\mathcal{L}(x,t) = \{1 + \exp\left[-\mu\cos(\omega_m t - k_m x) - \mu\cos(\pi \gamma)\right]\}^{-1}$$
 (S26)

where the c and ρ are the sound velocities and air density in the tube, c_n and ρ_n are the sound velocity and air density at nth unit cell, μ is the logistic growth rate which is 5 in this simulation, and γ is the exposed rate of unit cell which is 0.25. PML with 200 mm length is applied at both sides of the tube as shown in Fig. S4. The length of the metamaterials is 600 mm, consisting of 15-unit cells.

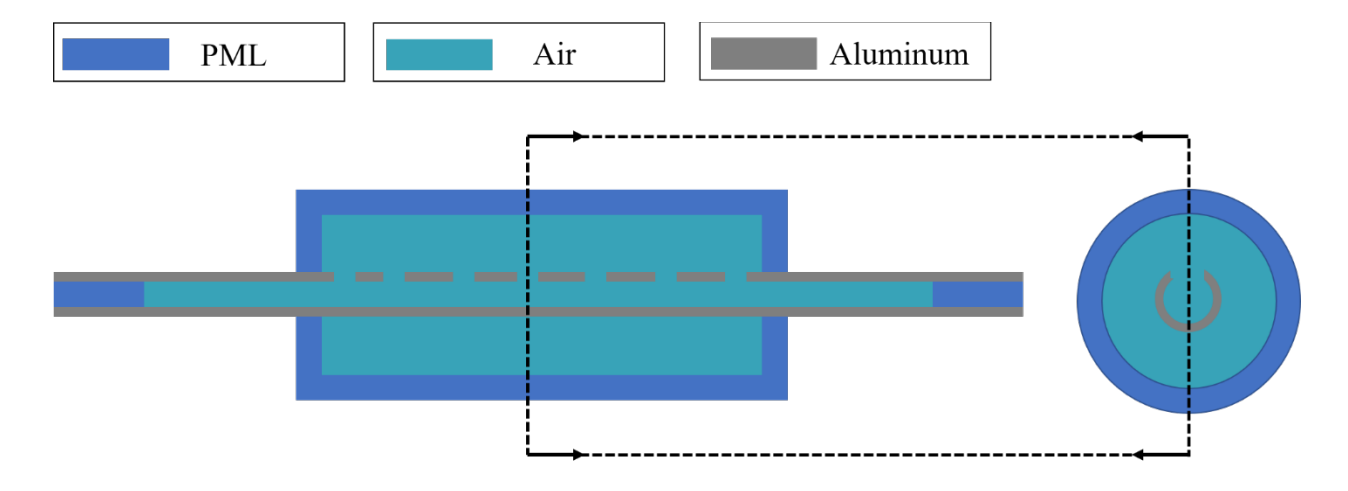


FIG. S4. Simulation diagram of the tube with the periodic ESs and details of the modulated layer.

In order to verify the nonreciprocal transmission in the tube, we use the tone burst signal. As shown in Fig. S5, clearly with a larger modulation speed, the nonreciprocal transmission is much clearer than that with a small modulation speed. A realistic experimental setup for realizing the phenomenon shown in Fig. 2 should be the same device shown in Fig. 3 in the main text. The

[Type here]

incident signals in Fig. 2(b) and Fig. S5 from the input side are a tone burst signal, covering from 3 to 7 kHz in the frequency domain. The modulation speed and direction of the acoustic tube waveguide can be easily tuned by adjusting the rotating speed and direction of the motor. The collected time-domain data from the output side then can be converted through Fourier transform into frequency spectra for all the modulation speed and direction combinations.

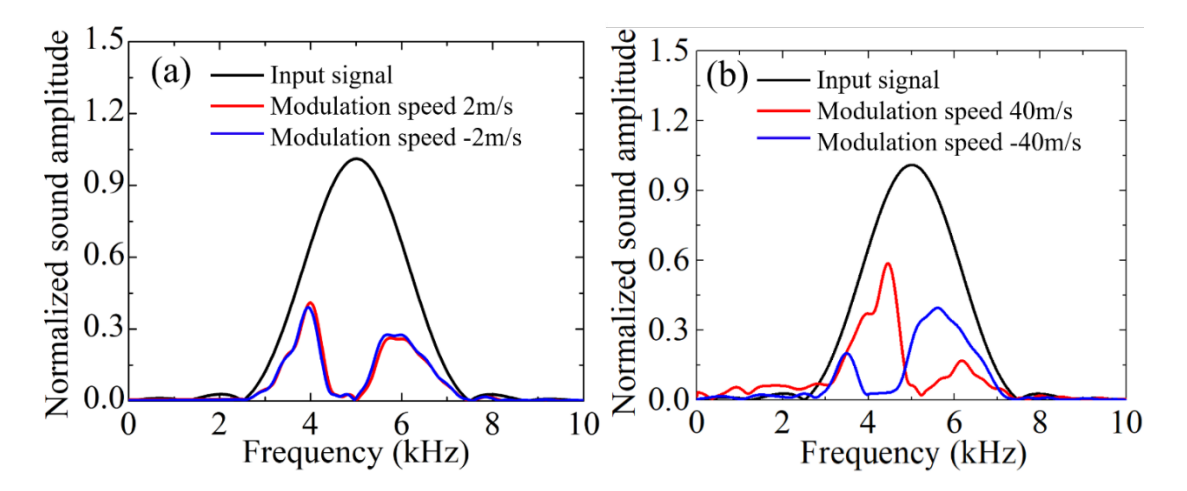


FIG. S5. Normalized sound amplitudes of the boundary-varying tube vs. incidental frequencies (a) with a modulation speed $c_m = \pm 2$ m/s, (b) with a modulation speed $c_m = \pm 40$ m/s.

The FIG. S5 shows the time-domain result discussed in FIG. 4. The blackline and redline are modulations with speed 10 m/s and -10 m/s.

To avoid impractical computing times, we used larger discretization time steps (see Fig. S6) in the simulation than in the experimental test. This why the peak width of the simulation result (Fig. 4b) is larger than in the experimental measurements in Fig. 4c. However, the central frequencies of the peaks still match very well between the simulations and experiments.

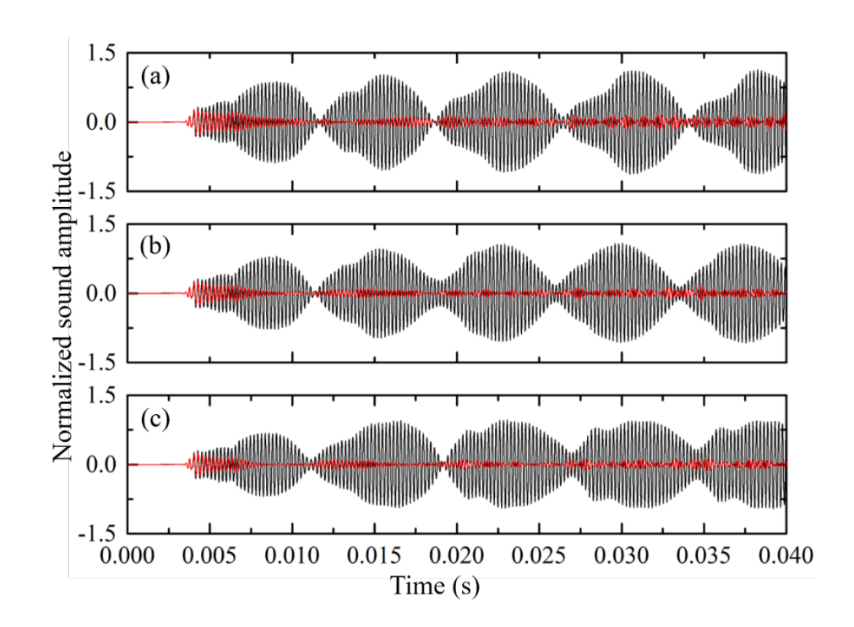


FIG. S6. The time-domain result of normalized sound amplitudes with a modulation speed 10 m/s at frequency 4450 Hz, 4470 Hz, 4490 Hz. The blackline and redline are modulations with speed 10 m/s and -10 m/s.

Edge mode simulations

Fig. 5(a) shows the band structure obtained numerically using the FEM-based package COMSOL Multiphysics for the finite tube. In the simulations, the tube is composed of 15 unit cells and its total length is 600 mm. Fixed boundary conditions are applied at the two ends of this tube. Since only slow modulation is considered in this work, the continuous time evolution of the eigenstates of the finite tube can be broken into a set of t-dependent snapshot eigenstates. This dynamic problem then is seen as a quasi-static one, and each time instant therefore corresponds to a specific position of the ESs within the finite tube. In the current design, a CW rotation of the tube corresponds to the translation of the ESs in the forward direction from 0 to 20 mm, while a CCW rotation corresponds to the backward-directional translation from -20 to 0 mm, as shown in Fig. S7(a). Specifically, the evolution of the frequency spectrum for the forward-directional translation from 0 to 20 mm can be obtained by rotating the tube from positions (i) to (v) and solving the eigenvalue problem for each position (time) instant. Fig. S7(b) shows the simulation model with positions of ESs at five different time instants. For both forward- and backward-directional translations, the calculated eigenfrequencies at all position (time) instants contribute to the complete band diagram shown in Fig. S7(a).

[Type here]

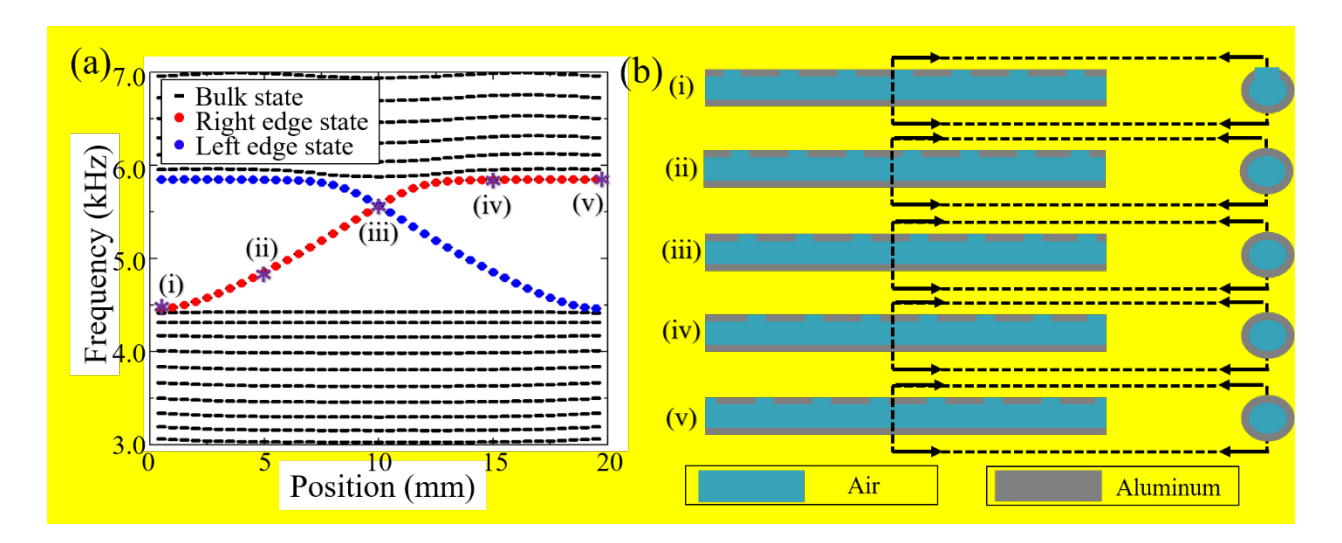


FIG. S7. Simulation diagram of the edge modes the tube with the periodic ESs and details of the modulated layer. (a) Evolution of eigenfrequencies of finite acoustic materials (15 unit cells) over one period of modulation under fixed boundary conditions on both ends. Five time instants are selected to conduct the eigenvalue analysis of the tube. (b) Schematics of the simulation models of the finite tube at the five selected time instants.

Section D: EXPERIMENTAL METHOD

Modulation experiment

The measurement tube is Mecanum's 4 microphone impedance tubes and data is collected by B&K 3050-A DAQ system. By spinning the outer helical tube driven by the gear system, the ESs translate in time, creating an apparent continuous translation of ESs along the tube continuously. The incident signal in the system we use is sine single frequency signal. We swept the sine single every 50 Hz and capture the transmission for every frequency. The end of the tube is open, which generates no reflection.

Edge mode experiments

To test the edge mode in the current system, we placed a block at one end of the inner tube to create a rigid boundary and placed a small speaker at the other end of the inner tube. The location of the block and the speaker inside the inner tube are fixed. To change the topological geometry of the boundary-varying tube, we rotated the outer tube. As the outer tube in boundary-varying tube is a helical tube, the ESs move forward or backward depending on whether it is the clockwise or counterclockwise rotation, as shown in Fig. S8.

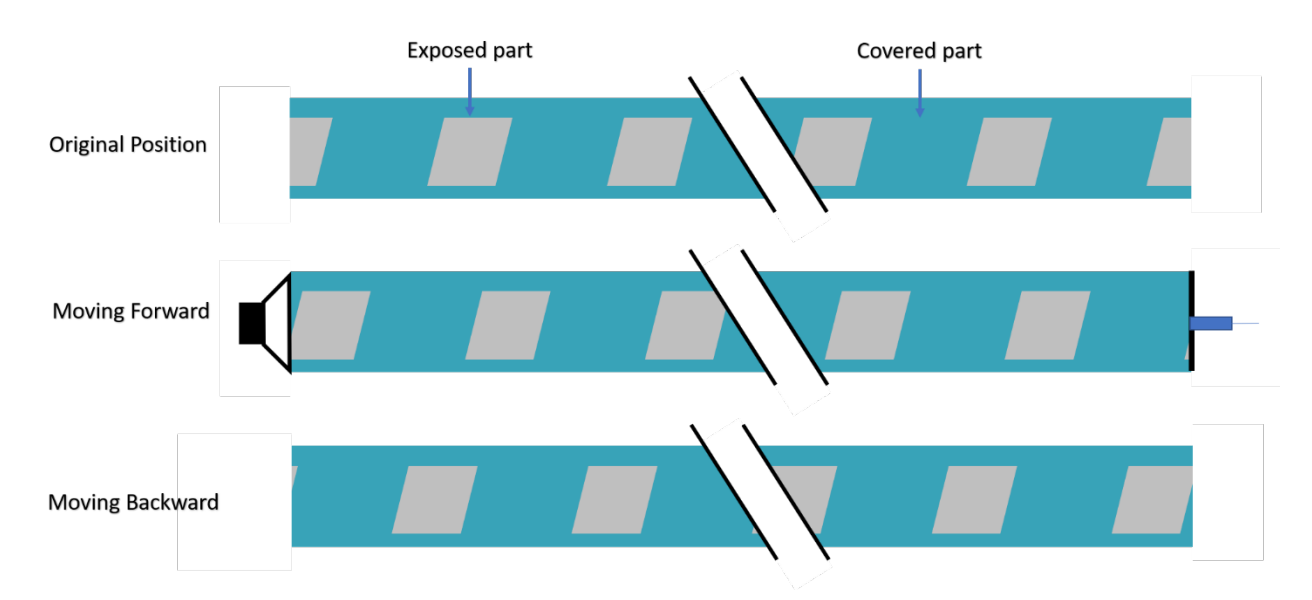


FIG. S8. Schematic diagrams of the experiments for examining the topological pumping involved in the modulated acoustic tube. For the clockwise rotation of the helical tube, the ESs move forward, while for the counterclockwise rotation, they move backward accordingly.

[Type here]

Indeed, evanescent waves could be incorrectly interpreted as edge modes. To demonstrate the difference between them, we tested two acoustic tubes under the boundary conditions (ii) and (iii), respectively (see also Fig. 5 in the main text). We define the measured region which is half of the tube without the excitation to distinguish the topological edge mode from the excitation signal. For the acoustic tube under the boundary condition (ii), we first excited at the left end and measured the acoustic field across the tube. We can observe the topological edge mode located at the right end, which is on the opposite side to the excitation [illustrated in Fig. S9(a)]. However, if we excited at the right end of the tube, no field concentration near the left end can be detected [see Fig. S9(b)]. This observation confirms that the acoustic tube under the boundary condition (ii) supports only the right topological edge mode. By contrast, the tube under the boundary condition (iii) only supports the left topological edge mode. As can be expected, the left edge mode is solely observed when the excitation is at the right edge [see Fig. S9(c)]. For the excitation at the left edge, no field concentration is measured near the right edge [see Fig. S9(d)]. Therefore, we can conclude that the edge fields localized near the tube ends other than where the source is placed are topological edge modes which exist within the band gap. In contrast, evanescent waves are only localized near the source and exponentially decay from the source.

In the experiments, we used a microphone to measure the acoustic field. The diameter of this microphone used in the experiment is 6 mm, much smaller than the wavelength of the field (68 mm). In this regard, the microphone in the tube does not perturb the field propagation.

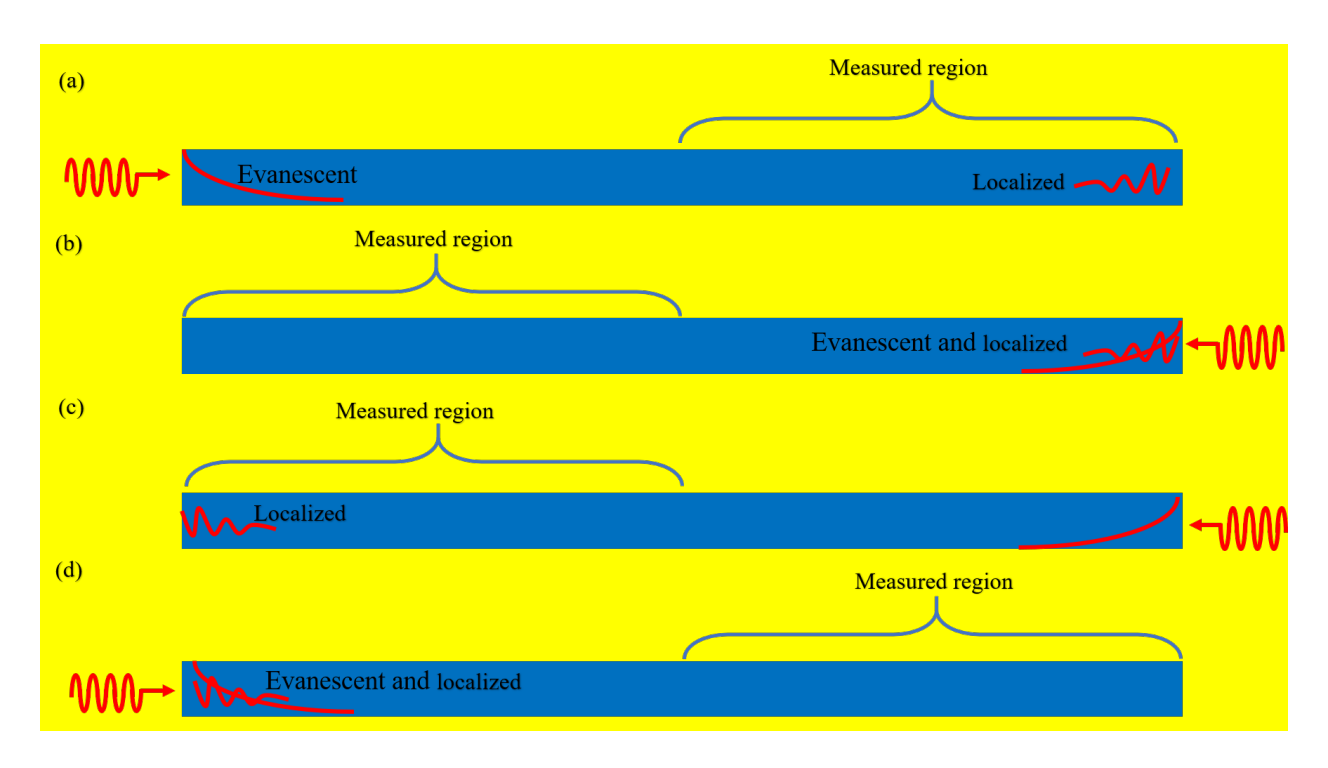


FIG. S9. Schematic diagram of the edge mode test: (a) excitation at the left end of the acoustic tube under the boundary condition (ii), (b) excitation at the right end of tube under the boundary condition (ii), (c) excitation at the right end of the acoustic tube under the boundary condition (iii), (b) excitation at the left end of the acoustic tube under the boundary condition (iii). The measured region indicate where the measurement is taken in each case.

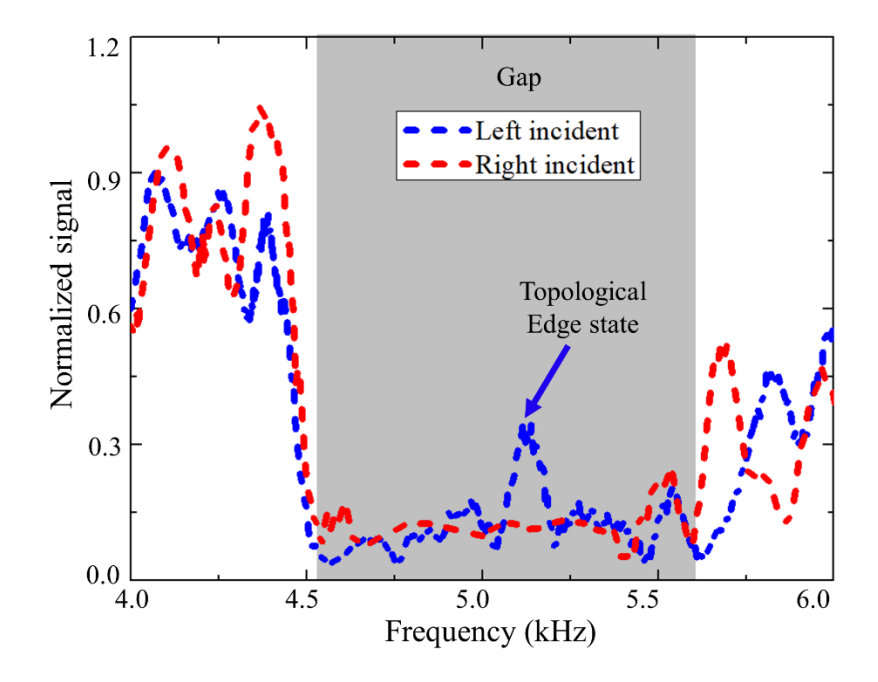


FIG. S10. Experimentally measured transmitted intensity spectra for phase condition (ii). The plots represent normalized acoustic response frequency spectrum measured by the microphone when the speaker/microphone was placed at right (blue dotted line) and left (red dotted line) sides.

Fig. S10 illustrates the frequency spectrum of measured signals at opposite side of the tube by microphone for phase condition (ii). As shown in Fig. S9, there is no obvious peak within the bandgap region when the system is excited from the right side, however, a transmission peak around 5.2 kHz within the bandgap is observed when the system is excited from the left side, proving the existence of the edge mode under phase condition (ii).

References

- [1] S.H. Lee, C.M. Park, Y.M. Seo, Z.G. Wang, and C.K. Kim, *Acoustic metamaterial with negative modulus*, J. Phys. Condens. Matter, **21**.175704 (2009).
- [2] H. Nassar, X.C. Xu, A.N. Norris, and G.L. Huang, *Modulated phononic crystals: Non-reciprocal wave propagation and Willis materials*, J. Mech. Phys. Solids, **101**.10 (2017).
- [3] T. Fukui, Y. Hatsugai, and H. Suzuki, *Chern numbers in discretized Brillouin zone: efficient method of computing (spin) Hall conductances.* J. Phys. Soc. Jpn. **74**, 1674 (2005)
- [4] H. Nassar, H. Chen, A.N. Norris, and G.L. Huang, *Quantization of band tilting in modulated* phononic crystals Phys. Rev. B, **97**, 014305 (2018).

[†]Author contributed equally

^{*}Email:huangg@missouri.edu